INTERNATIONAL JOURNAL FOR NUMERICAL METHODS IN ENGINEERING
Int. J. Numer. Meth. Engng 2003; **56**:1315–1334 (DOI: 10.1002/nme.614)

A non-iterative finite element method for inverse heat conduction problems

Xianwu Ling, Russell G. Keanini*,† and H. P. Cherukuri

Department of Mechanical Engineering and Engineering Science, The University of North Carolina at Charlotte, Charlotte, NC 28223, U.S.A.

SUMMARY

A non-iterative, finite element-based inverse method for estimating surface heat flux histories on thermally conducting bodies is developed. The technique, which accommodates both linear and non-linear problems, and which sequentially minimizes the least squares error norm between corresponding sets of measured and computed temperatures, takes advantage of the linearity between computed temperatures and the instantaneous surface heat flux distribution. Explicit minimization of the instantaneous error norm thus leads to a linear system, i.e. a matrix normal equation, in the current set of nodal surface fluxes. The technique is first validated against a simple analytical quenching model. Simulated low-noise measurements, generated using the analytical model, lead to heat transfer coefficient estimates that are within 1% of actual values. Simulated high-noise measurements lead to h estimates that oscillate about the low-noise solution. Extensions of the present method, designed to smooth oscillatory solutions, and based on future time steps or regularization, are briefly described. The method's ability to resolve highly transient, early-time heat transfer is also examined; it is found that time resolution decreases linearly with distance to the nearest subsurface measurement site. Once validated, the technique is used to investigate surface heat transfer during experimental quenching of cylinders. Comparison with an earlier inverse analysis of a similar experiment shows that the present method provides solutions that are fully consistent with the earlier results. Although the technique is illustrated using a simple one-dimensional example, the method can be readily extended to multidimensional problems. Copyright © 2003 John Wiley & Sons, Ltd.

KEY WORDS: heat conduction; inverse methods; non-iterative methods; heat-transfer coefficient; finite element method

1. INTRODUCTION

Inverse heat conduction problems (IHCP) seek to determine surface heat flux or temperature histories, thermophysical properties, contact conductances, volumetric heat sources, or initial

*Correspondence to: R. G. Keanini, Department of Mechanical Engineering, The University of North Carolina at Charlotte, 9201 University City Blvd, Charlotte, NC 28223-0001, U.S.A.
†E-mail: rkeanini@uncc.edu

Contract/grant sponsor: National Science Foundation; contract/grant number: DMI-9820880

Received 24 July 2001
Revised 25 March 2002
Accepted 22 May 2002

conditions in or on a conducting body, given interior temperature measurements (see, e.g., References [1, 2]). Considering the classical problem of estimating a spatially varying surface heat flux history, parameterized by the vector $\tilde{\mathbf{q}}(t)$, the vector is generally determined by minimizing some error measure, S, between a set of measured temperatures, $\tilde{\mathbf{Y}}$, and a corresponding set of calculated temperatures, $\tilde{\boldsymbol{\theta}}$. Typically, S comprises a least squares error norm

$$S=(\tilde{\mathbf{Y}}-\tilde{\boldsymbol{\theta}})^{\mathrm{T}}(\tilde{\mathbf{Y}}-\tilde{\boldsymbol{\theta}}) \tag{1}$$

where modified forms of this definition are used when measurement errors are not equal [1] or when measurements are approximately continuous in time. Likewise, various regularization terms can be added to circumvent ill-conditioning [1–3]. The data included in S can include all measurements, appropriate for whole (time) domain solutions, or small subsets of available data, appropriate in sequential solution schemes; since $\tilde{\boldsymbol{\theta}}$ depends on $\tilde{\mathbf{q}}$, S has the same implicit functional dependence.

Two general approaches are used in minimizing S. *Iterative methods* determine $\tilde{\mathbf{q}}$ by iteratively minimizing S via a numerical minimization scheme, e.g. the conjugate gradient method [1, 4], dynamic programming techniques [5], the Levenberg–Marquardt algorithm [1], or the multidimensional simplex method [6]. Here, $\tilde{\mathbf{q}}$ is iteratively altered until some convergence criterion is satisfied. *Non-iterative methods*, by contrast, minimize S by explicitly forming the system

$$\frac{\partial S}{\partial \tilde{\mathbf{q}}}=\mathbf{0} \tag{2}$$

where the objective is to derive a linear system, called the *matrix normal equation*, in $\tilde{\mathbf{q}}$ [2]. Once derived, the matrix normal equation can be solved directly and non-iteratively for $\tilde{\mathbf{q}}$. Although much recent work has focused on iterative solution techniques, this article will focus on the less-studied problem of non-iterative, finite element-based solution methods.

In order to derive a matrix normal equation, a crucial preliminary step must be taken, viz, an explicit linear relationship between $\tilde{\boldsymbol{\theta}}$ and $\tilde{\mathbf{q}}$, called the *standard form temperature equation*, must be derived [2]. Beck *et al.* [2] have given a number of forms for the standard temperature equation, obtained in most cases by either Taylor expanding $\tilde{\boldsymbol{\theta}}(\tilde{\mathbf{q}})$ about some trial temperature and flux vector, $\boldsymbol{\theta}^*$ and $\mathbf{q}^*$, respectively, or, in geometrically simple, linear problems, via Duhamel integrals. However, the methods used (e.g. Duhamel's method) are either appropriate only to linear problems, or are limited to one-dimensional heat conduction problems. With regard to finite element versions of the standard temperature equation, it appears that while a special one-dimensional case has been obtained [2], more general forms, suitable for multidimensional problems and spatially varying flux distributions, have not been reported.

Once a standard form temperature equation has been obtained, an immediate benefit is realized: the sensitivity or Jacobian matrix, $\tilde{\mathbf{X}}=[\partial\tilde{\boldsymbol{\theta}}^{\mathrm{T}}/\partial\tilde{\mathbf{q}}]^{\mathrm{T}}$, which is central to most iterative and non-iterative solution methods, can be derived in explicit form. This eliminates the need for separate numerical calculations of $\tilde{\mathbf{X}}$, based, for example, on solutions of modified forms of the direct problem [1] or on explicit and computationally expensive finite difference approximations of each component, $\tilde{X}_{ij}$ [1, 2]. This feature, combined with the non-iterative nature of these solution techniques, makes these methods potentially attractive in process control and thermal reconstruction applications requiring fast inverse solutions [7].

In this paper, a non-iterative, finite element-based method is developed for solving the IHCP. Here, the unknown instantaneous surface flux distribution, parameterized by the vector, $\tilde{\mathbf{q}}^{n+1}$, is determined sequentially (at each instant, $t=t^{n+1}$), based on a set of instantaneous temperature measurements, $\tilde{\mathbf{Y}}^{n+1}$. The method takes advantage of the fact that the direct FEM model governing conduction within the conducting body can be stated in a form that is *linear* in $\tilde{\mathbf{q}}^{n+1}$. Based on this linearity, a general FEM standard form temperature equation can be derived which is appropriate for non-linear multidimensional problems subject to arbitrary surface flux distributions. A corresponding, non-regularized matrix normal equation is then obtained and used to derive a relatively simple inverse solution algorithm.

Since the method must be capable of accurately estimating highly transient heat transfer histories during quenching, it is first illustrated and validated using a simple one-dimensional quenching model. While particular attention is given to determining the technique's ability to resolve early-time heat transfer, sensitivity to measurement error and solution time-step size are also briefly examined. Once validated, the procedure is used to determine surface heat transfer during experimental quenching of long cylinders; a comparison with an earlier inverse solution of a similar experimental problem is also presented. Finally, a modified two-step algorithm, incorporating future data and designed to reduce ill-conditioning in the matrix normal equation, is developed and tested.

2. INVERSE METHOD FORMULATION

In this section, the inverse problem to be solved is defined and then the direct heat conduction problem governing the computed temperature vector $\tilde{\boldsymbol{\theta}}$ in (1) is described, and finally the inverse solution procedure is formulated.

2.1. Inverse problem definition

Consider a continuous two-dimensional region Ω bounded by the curve $\Gamma=\Gamma_1\cup\Gamma_2$, where Γ_1 is the portion of Γ subject to known temperature and/or heat flux conditions and where Γ_2 is the portion of the boundary on which thermal conditions are unknown. [Although the formulation can be readily extended to three-dimensional problems, for simplicity and consistency with experiments described below, we only consider the two-dimensional case.] Assume that Ω is discretized by a contiguous set of finite elements and let $\mathbf{q}^{n+1}$ represent the set of instantaneous nodal (normal) heat fluxes extant on Γ_2:

$$\mathbf{q}^{n+1}=\left[q_1^{n+1},q_2^{n+1},\ldots,q_J^{n+1}\right]^{\mathrm{T}} \tag{3}$$

where q_i^{n+1} is the nodal flux at the ith node on Γ_2, and where superscripts denote the time index, and J is the total number of nodes on Γ_2. [Note, i is a local index spanning the J nodes on Γ_2.] Now, let the unknown instantaneous flux distribution be parameterized using K of the J members comprising $\mathbf{q}^{n+1}$, where the K chosen nodal fluxes define a vector $\tilde{\mathbf{q}}^{n+1}$:

$$\tilde{\mathbf{q}}^{n+1}=\left[\tilde{q}_1^{n+1},\tilde{q}_2^{n+1},\ldots,\tilde{q}_K^{n+1}\right]^{\mathrm{T}} \tag{4}$$

and $K\leqslant J$. When $K<J$, the $J-K$ nodal fluxes not included in $\tilde{\mathbf{q}}^{n+1}$ are determined by interpolation on $\tilde{\mathbf{q}}^{n+1}$. In order to determine the vector $\tilde{\mathbf{q}}^{n+1}$, we assume that instantaneous

time-varying temperature measurements, $\tilde{\mathbf{Y}}^{n+1}$, are available, obtained at I interior nodes on Ω:

$$\tilde{\mathbf{Y}}^{n+1} = \left[\tilde{Y}_1^{n+1}, \tilde{Y}_2^{n+1}, \ldots \tilde{Y}_I^{n+1}\right]^{\mathrm{T}} \tag{5}$$

where $\tilde{Y}_i^{n+1}$ is the measured temperature at the ith measurement site and where i is again a local index (over the measurement sites).

Given the above definitions, we now state the inverse problem as follows: determine the instantaneous heat flux distribution on Γ_2, represented by $\tilde{\mathbf{q}}^{n+1}$, given the set of instantaneous measurements, $\tilde{\mathbf{Y}}^{n+1}$.

2.2. Direct heat conduction problem

Solution of the inverse problem requires solution of the direct heat conduction problem on Ω. Thus, in the case where no heat sources are present, heat conduction on Ω is governed by the non-linear heat conduction equation

$$\nabla \cdot (k \nabla \theta) = \rho c \frac{\partial \theta}{\partial t} \tag{6}$$

subject to the boundary conditions

$$\theta = \theta_\infty \quad \text{on } \Gamma_1 \tag{7}$$

and

$$k \nabla \theta \cdot \mathbf{n} = q \quad \text{on } \Gamma_2 \tag{8}$$

where for simplicity, we assume that only temperatures are specified on Γ_1. The initial condition is

$$\theta(\mathbf{X}, 0) = \theta_0(\mathbf{X}) \tag{9}$$

where $\mathbf{X} = [x, y, z]$. In general, ρ, c and k are temperature dependent, while q is time and space dependent.

The direct problem is solved using the Galerkin finite element method, where the resulting system of equations is given by

$$(\mathbf{M} + \Delta t \gamma \mathbf{K})\boldsymbol{\theta}^{n+1} = [\mathbf{M} - \Delta t(1-\gamma)\mathbf{K}]\boldsymbol{\theta}^n + \Delta t \gamma \mathbf{f}^{n+1} + \Delta t(1-\gamma)\mathbf{f}^n \tag{10}$$

and where components of the element capacity and stiffness matrices are given by

$$M_{ij}^{\mathrm{e}} = \int_{\Omega_{\mathrm{e}}} \rho c N_i N_j \, \mathrm{d}\Omega \tag{11}$$

$$K_{ij}^{\mathrm{e}} = \int_{\Omega_{\mathrm{e}}} k N_{i,\alpha} N_{j,\alpha} \, \mathrm{d}\Omega \tag{12}$$

Note that Ω_{e} is the element volume, N_i is a finite element interpolation function, and summation over α ($=1, 2$, for two-dimensional problems) is implied. It is important to note also that in non-linear problems (where temperature variations are large enough to induce significant

thermophysical property variations), quasilinearization [1, 2] is used to evaluate $\mathbf{M}$ and $\mathbf{K}$. Thus, the magnitudes of ρ, c, and k, at the current time step are evaluated using the temperature solution, $\boldsymbol{\theta}^n$, from the previous time step. In all cases, superscripts on $\mathbf{M}$ and $\mathbf{K}$ are suppressed for clarity. Components of the element force vector are given by

$$f_i^{\mathrm{e}} = \int_{\Gamma_{\mathrm{e}}} N_i q \, \mathrm{d}\Gamma \tag{13}$$

where Γ_{e} is the element boundary and where the time index has again been suppressed.

Here, the implicit one step Euler backward difference method is employed. Thus, by setting $\gamma = 1$ in Equation (10), we obtain

$$(\mathbf{M} + \Delta t_0 \mathbf{K})\boldsymbol{\theta}^{n+1} = \mathbf{M}\boldsymbol{\theta}^n + \Delta t_0 \mathbf{f}^{n+1} \tag{14}$$

where $\Delta t_0 = t^{n+1} - t^n$ is the current time step.

2.3. *Inverse method*

The unknown instantaneous flux distribution, parameterized by the vector $\tilde{\mathbf{q}}^{n+1}$, is determined by minimizing an instantaneous error norm, S^{n+1}, with respect to $\tilde{\mathbf{q}}^{n+1}$, where S^{n+1} is given by

$$S^{n+1} = (\tilde{\mathbf{Y}}^{n+1} - \tilde{\boldsymbol{\theta}}^{n+1})^{\mathrm{T}} (\tilde{\mathbf{Y}}^{n+1} - \tilde{\boldsymbol{\theta}}^{n+1}) \tag{15}$$

and where the vector of computed instantaneous measurement site temperatures is expressed as

$$\tilde{\boldsymbol{\theta}}^{n+1} = \left[\tilde{\theta}_1^{n+1}, \tilde{\theta}_2^{n+1}, \ldots \tilde{\theta}_I^{n+1} \right]^{\mathrm{T}} \tag{16}$$

In order to calculate $\tilde{\boldsymbol{\theta}}^{n+1}$, the instantaneous global temperature vector, $\boldsymbol{\theta}^{n+1}$, is computed using Equation (14):

$$\boldsymbol{\theta}^{n+1} = \boldsymbol{\psi}^n + \Delta t_0 \mathbf{U} \mathbf{f}^{n+1} \tag{17}$$

where

$$\mathbf{U} = (\mathbf{M} + \Delta t_0 \mathbf{K})^{-1} \tag{18}$$

and

$$\boldsymbol{\psi}^n = (\mathbf{M} + \Delta t_0 \mathbf{K})^{-1} \mathbf{M} \boldsymbol{\theta}^n \tag{19}$$

It is important to note that the system represented by Equation (14) is a *condensed system* in which all primary boundary conditions (on Γ_1) have been introduced and used to reduce the global system. Alternative algorithms can be developed for non-condensed systems, but are somewhat more involved.

Minimizing S^{n+1} with respect to $\tilde{\mathbf{q}}^{n+1}$, we obtain the following system of equations:

$$\tilde{\mathbf{X}}^{\mathrm{T}} (\tilde{\mathbf{Y}}^{n+1} - \tilde{\boldsymbol{\theta}}^{n+1}) = \mathbf{0} \tag{20}$$

where $\tilde{\mathbf{X}}$ is the $I \times K$ sensitivity coefficient matrix, having elements given by

$$\tilde{X}_{ij} = \frac{\partial \tilde{\theta}_i^{n+1}}{\partial \tilde{q}_j^{n+1}} \tag{21}$$

and where superscripts on $\tilde{X}_{ij}$ are again suppressed.

We now show that the system in (20) can be expressed as an explicit linear system in $\tilde{\mathbf{q}}^{n+1}$, i.e. that a matrix normal equation can be derived. This crucial step will provide the basis for constructing a non-iterative inverse solution scheme for determining $\tilde{\mathbf{q}}^{n+1}$. In order to show this, we make the key observation that the global force vector $\mathbf{f}^{n+1}$ can be expressed as a linear function of $\tilde{\mathbf{q}}^{n+1}$. Although this feature is generally recognized, it apparently has not been exploited in developing FEM-based inverse solution methods for the IHCP. Thus, we express $\mathbf{f}^{n+1}$ as

$$\mathbf{f}^{n+1} = \tilde{\mathbf{D}}\tilde{\mathbf{q}}^{n+1} + \mathbf{c} \tag{22}$$

where elements of $\tilde{\mathbf{D}}$, given by

$$\tilde{D}_{Pj} = \frac{\partial f_P^{n+1}}{\partial \tilde{q}_j^{n+1}} \tag{23}$$

are constants determined by the finite element discretization, and where the constant vector $\mathbf{c}$, produced by condensation, is determined by the known temperature distribution on Γ_1. In (23), upper-case subscripts refer to global node numbers while lower-case subscripts again refer to the local index over the K members of $\tilde{\mathbf{q}}^{n+1}$. Note that the dimensions of $\tilde{\mathbf{D}}$ and $\mathbf{c}$ are $N \times K$ and $N \times 1$, respectively, where N is the total number of nodes on Ω.

Having expressed $\mathbf{f}^{n+1}$ as a linear function of $\tilde{\mathbf{q}}^{n+1}$, we can now readily show that the computed measurement site temperatures, $\tilde{\boldsymbol{\theta}}^{n+1}$, are likewise linear in $\tilde{\mathbf{q}}^{n+1}$. Thus, substituting (22) into (17), we obtain the standard form temperature equation:

$$\tilde{\boldsymbol{\theta}}^{n+1} = \tilde{\boldsymbol{\psi}}^n + \Delta t_0 \tilde{\mathbf{U}}[\tilde{\mathbf{D}}\tilde{\mathbf{q}}^{n+1} + \mathbf{c}] \tag{24}$$

where elements of $\tilde{\mathbf{U}}$ are related to those in $\mathbf{U}$ by $\tilde{U}_{iP} = U_{GP}$, and where the local index i (spanning the I measurement sites) maps to global node G. Note too that P is a global node number. Likewise, elements of $\tilde{\boldsymbol{\psi}}^n$ are related to those in $\boldsymbol{\psi}^n$ by $\tilde{\psi}_i^n = \psi_G^n$. Thus, the reduced matrix $\tilde{\mathbf{U}}$ has dimensions $I \times N$, while $\tilde{\boldsymbol{\psi}}^n$ is $I \times 1$. Given (24), we can now determine the sensitivity coefficients, $\tilde{X}_{ij}$, in explicit form. Thus, from (21) and (24) we obtain

$$\tilde{\mathbf{X}} = \Delta t_0 \tilde{\mathbf{U}}\tilde{\mathbf{D}} \tag{25}$$

or in expanded form,

$$\tilde{X}_{ij} = \Delta t_0 \sum_{P=1}^{N} \tilde{U}_{iP}\tilde{D}_{Pj} \tag{26}$$

Having derived explicit relationships for $\tilde{\boldsymbol{\theta}}^{n+1}$ and $\tilde{\mathbf{X}}$, we can now use (24) and (25) in (20) to prove our initial assertion, viz, (20) represents a linear system in $\tilde{\mathbf{q}}^{n+1}$:

$$\tilde{\mathbf{X}}^{\mathrm{T}}\tilde{\mathbf{X}}\tilde{\mathbf{q}}^{n+1} + \tilde{\mathbf{X}}^{\mathrm{T}}[\tilde{\boldsymbol{\psi}}^n + \mathbf{g} - \tilde{\mathbf{Y}}^{n+1}] = \mathbf{0} \tag{27}$$

where $\mathbf{g}=\Delta t_0\tilde{\mathbf{U}}\mathbf{c}$. Equation (27) is an important result since it represents the general, non-regularized matrix normal equation for FEM-based inverse solutions to the IHCP. Together with the explicit expression obtained for $\tilde{\mathbf{X}}$, Equation (25), Equation (27) provides a basis for developing efficient, relatively simple, non-iterative solution procedures.

In order to obtain a solution for $\tilde{\mathbf{q}}^{n+1}$, the coefficient matrix $\tilde{\mathbf{X}}^{\mathrm{T}}\tilde{\mathbf{X}}$, must be non-singular, i.e. the *identifiability condition* [1] $\tilde{\mathbf{X}}^{\mathrm{T}}\tilde{\mathbf{X}} \neq \mathbf{0}$, must be satisfied. In cases where ill-conditioning must be accommodated, regularization and/or introduction of future data can be used. Section 2.4 discusses these points in more detail.

Based on the preceding development, we propose the following inverse solution algorithm. Given $\boldsymbol{\theta}^n$, $\tilde{\mathbf{Y}}^{n+1}$, $\mathbf{M}$, $\mathbf{K}$, and $\mathbf{c}$, $\tilde{\mathbf{q}}^{n+1}$ is first determined using Equation (27). Given $\tilde{\mathbf{q}}^{n+1}$, $\mathbf{f}^{n+1}$ is then calculated from Equation (22) and in turn, used in Equation (17) to obtain $\boldsymbol{\theta}^{n+1}$. It is important to note that the present algorithm presumes that the initial temperature distribution, $\boldsymbol{\theta}^0$, is known. While this is a reasonable assumption in problems such as quenching, in cases where $\boldsymbol{\theta}^0$ is unknown, a separate inverse solution (likely involving iteration) may be required.

As a closing aside, it is interesting to note that $\tilde{\mathbf{X}}$ depends on the positions of three sets of nodes: the I measurement node points, the J surface nodes on Γ_2, and the K nodes chosen from the second set. Thus, optimization of the arrangement of the three node sets is possible, for example, as a way to maximize and/or decorrelate sensitivity coefficients. Further study of this question will be discussed in a future publication.

2.4. Modified versions of the basic algorithm—future time steps and regularization

A *two-step* algorithm which incorporates data from one future time increment has also been developed and tested. The first step is used to compute an approximate solution for the instantaneous temperature field, which we will denote as $\tilde{\boldsymbol{\theta}}_1^{n+1}$. This is accomplished by first calculating an initial solution for $\tilde{\mathbf{q}}^{n+1}$, denoted as $\tilde{\mathbf{q}}_1^{n+1}$, using the basic inverse algorithm described in Sections 2.1–2.3. Given $\tilde{\mathbf{q}}_1^{n+1}$, $\tilde{\boldsymbol{\theta}}_1^{n+1}$, is then calculated as described in the penultimate paragraph of Section 2.3.

The second step, designed to improve both $\tilde{\mathbf{q}}_1^{n+1}$ and $\tilde{\boldsymbol{\theta}}_1^{n+1}$ using data at t^{n+2} (i.e. using $\tilde{\mathbf{Y}}^{n+2}$), is formulated as follows. We first set $\gamma=0$ in Equation (10) to obtain:

$$\mathbf{M}\boldsymbol{\theta}^{n+2}=(\mathbf{M}-\Delta t_1\mathbf{K})\boldsymbol{\theta}_1^{n+1}+\Delta t_1\mathbf{f}^{n+1} \tag{28}$$

where temperature-dependent $\mathbf{M}$ and $\mathbf{K}$ are again determined using $\boldsymbol{\theta}^n$ and where $\Delta t_1 = t^{n+2}-t^{n+1}$. Solving (28) for $\boldsymbol{\theta}^{n+2}$ leads to

$$\boldsymbol{\theta}^{n+2}=\boldsymbol{\psi}_1^{n+1}+\Delta t_1\mathbf{V}\mathbf{f}^{n+1} \tag{29}$$

where

$$\mathbf{V}=\mathbf{M}^{-1} \tag{30}$$

and

$$\boldsymbol{\psi}_1^{n+1}=\mathbf{M}^{-1}(\mathbf{M}-\Delta t_1\mathbf{K})\boldsymbol{\theta}_1^{n+1} \tag{31}$$

Following the same steps outlined in (20)–(25) above, we then obtain the following linear system in $\tilde{\mathbf{q}}^{n+1}$:

$$\tilde{\mathbf{X}}_1^{\mathrm{T}}\tilde{\mathbf{X}}_1\tilde{\mathbf{q}}^{n+1}+\tilde{\mathbf{X}}_1^{\mathrm{T}}\left[\tilde{\boldsymbol{\psi}}_1^{n+1}+\mathbf{g}_1-\tilde{\mathbf{Y}}^{n+2}\right]=\mathbf{0} \tag{32}$$

where

$$\tilde{\mathbf{X}}_1 = \Delta t_1 \tilde{\mathbf{V}} \tilde{\mathbf{D}} \tag{33}$$

and

$$\mathbf{g}_1 = \Delta t_1 \tilde{\mathbf{V}} \mathbf{c} \tag{34}$$

Here, as before, elements of the reduced matrix $\tilde{\mathbf{V}}$ and the reduced vector $\tilde{\boldsymbol{\psi}}_1^{n+1}$ are related to global $\mathbf{V}$ and $\boldsymbol{\psi}_1^{n+1}$ through $\tilde{V}_{iP} = V_{GP}$ and $\tilde{\psi}_{1_i}^{n+1} = \psi_{1_G}^{n+1}$, and where again local index i maps to global node G and P is a global node number.

Although (32) could be solved directly for $\tilde{\mathbf{q}}^{n+1}$, in order to improve system conditioning we instead combine (32) with (27) to obtain

$$(\tilde{\mathbf{X}}^{\mathrm{T}}\tilde{\mathbf{X}} + \tilde{\mathbf{X}}_1^{\mathrm{T}}\tilde{\mathbf{X}}_1)\tilde{\mathbf{q}}^{n+1} + \tilde{\mathbf{X}}^{\mathrm{T}}[\tilde{\boldsymbol{\psi}}^n + \mathbf{g} - \tilde{\mathbf{Y}}^{n+1}] + \tilde{\mathbf{X}}_1^{\mathrm{T}}[\tilde{\boldsymbol{\psi}}_1^n + \mathbf{g}_1 - \tilde{\mathbf{Y}}^{n+2}] = \mathbf{0} \tag{35}$$

Once $\tilde{\mathbf{q}}^{n+1}$ is thus computed, $\mathbf{f}^{n+1}$ is determined using (22) and the final solution for $\boldsymbol{\theta}^{n+1}$ is calculated from (17).

Although this modified algorithm uses data from one future time step [2] as a means of stabilizing the inverse solution, our tests described below indicate no significant difference between solutions obtained by this approach and those obtained the basic algorithm described in Sections 2.1–2.3.

As an alternative to the use of future data, inverse solutions can be smoothed using Tikhonov regularization. The most general expression for S in this case is [2]

$$S = (\mathbf{Y} - \boldsymbol{\theta})^{\mathrm{T}}(\mathbf{Y} - \boldsymbol{\theta}) + \alpha[W_0(\mathbf{H}_0\mathbf{q})^{\mathrm{T}}\mathbf{H}_0\mathbf{q} + W_1(\mathbf{H}_1\mathbf{q})^{\mathrm{T}}\mathbf{H}_1\mathbf{q} + W_2(\mathbf{H}_2\mathbf{q})^{\mathrm{T}}\mathbf{H}_2\mathbf{q}] \tag{36}$$

where W_0, W_1, and W_2 are weight factors for zeroth, first and second order regularization, respectively, α is a regularization parameter, and $\mathbf{H}_0$, $\mathbf{H}_1$, and $\mathbf{H}_2$ are problem-specific matrices determined by the number of parameters defining $\mathbf{q}$ (see Reference [2]). Noting that in the present sequential algorithm, $\mathbf{q} = \tilde{\mathbf{q}}^{n+1}$, $\mathbf{Y} = \tilde{\mathbf{Y}}^{n+1}$, $\boldsymbol{\theta} = \tilde{\boldsymbol{\theta}}^{n+1}$, and $S = S^{n+1}$, then it is clear that the system $\partial S/\partial \tilde{\mathbf{q}}^{n+1} = \mathbf{0}$ obtained from Equation (36) is again linear in $\tilde{\mathbf{q}}^{n+1}$.

3. NUMERICAL TESTS

3.1. Generation of simulated data for validating the inverse method

In order to validate the inverse method, we first generate temperature data using a simplified analytical model of quenching. In particular, we assume that an infinite cylinder of radius R ($=0.0065$ m) at a uniform initial temperature θ_0 ($=850°$C) is rapidly immersed in a stagnant fluid at θ_∞ ($=40°$C). The heat transfer coefficient h is chosen as $1000\ \mathrm{W m^{-2}\ K^{-1}}$ and constant thermophysical properties, representative of high temperature nickel-based alloys, are used ($k = 20.6\ \mathrm{W\ m^{-1}\ K^{-1}}$, $\rho = 8050\ \mathrm{kg\ m^{-3}}$, $c = 565\ \mathrm{J\ kg^{-1}\ K^{-1}}$). The solution, stated in terms of dimensionless variables, is given by [8]:

$$\bar{\theta}(\bar{r}, \bar{t}) = 2B_i \sum_{m=1}^{\infty} \mathrm{e}^{-\bar{\lambda}_m^2 \bar{t}} \frac{J_0(\bar{\lambda}_m \bar{r})}{(B_i^2 + \bar{\lambda}_m^2) J_0(\bar{\lambda}_m)} \tag{37}$$

where

$$B_i = \frac{hR}{k} \tag{38}$$

$$\bar{r} = \frac{r}{R} \tag{39}$$

$$\bar{t} = \frac{\alpha t}{R^2} \tag{40}$$

$$\bar{\theta} = \frac{\theta - \theta_\infty}{\theta_0 - \theta_\infty} \tag{41}$$

and where $\bar{\lambda}_m$ are the eigenvalues satisfying

$$B_i J_0(\bar{\lambda}_m) = \bar{\lambda}_m J_1(\bar{\lambda}_m) \quad m = 1, 2, \ldots \tag{42}$$

Here J_0 and J_1 are zeroth order and first order Bessel functions of the first kind, respectively.

Using the above exact solution, noise-free data are generated at 500 equally spaced times at each measurement site, where site locations are described in the next subsection. The time interval, Δt_E, between generation of each simulated measurement is chosen as $\Delta t_E = 0.40\ \tau_D$, where τ_D, given by

$$\tau_D = \frac{\Delta R^2}{\alpha} \tag{43}$$

is the characteristic diffusive time scale between the surface and the nearest subsurface measurement site (located at a depth $\Delta R = 5 \times 10^{-4}$ m; see Section 3.2). This choice allows for well-resolved inverse solutions in time.

3.2. Finite element discretization

In order to illustrate and test the inverse procedure developed above and in order to provide a model for analysing multi-mode heat transfer during quenching experiments described below, we discretize the cylinder described in the last subsection using a row of axisymmetric isoparametric elements. The elements span the cylinder's radius and are assigned a fixed height H and fixed radial length $\Delta R (= R/13)$; see Figure 1. The model assumes that radial conduction dominates axial, which is valid for long, thin cylinders having negligible axial variations in surface heat transfer. In cases where surface heat transfer varies significantly in the axial direction, the finite element mesh would span the length of the cylinder. For purposes of illustration and consistency with experiments described below, we use the simple mesh shown in Figure 1.

In validation tests described in the next three subsections, pairs of simulated measurement sites are located at nodes 1 and 2, 7 and 8, 15 and 16, 23 and 24, and/or 25 and 26, as shown in Figure 1. All tests are run using at least one pair of measurement sites, with various combinations tested, including all five pairs. The objective in all cases will be to solve for the time-dependent fluxes, q_{27}^{n+1} and q_{28}^{n+1}, given measured temperatures, $\tilde{\mathbf{Y}}^{n+1}$. Details illustrating application of the inverse formulation to this problem and to the experimental

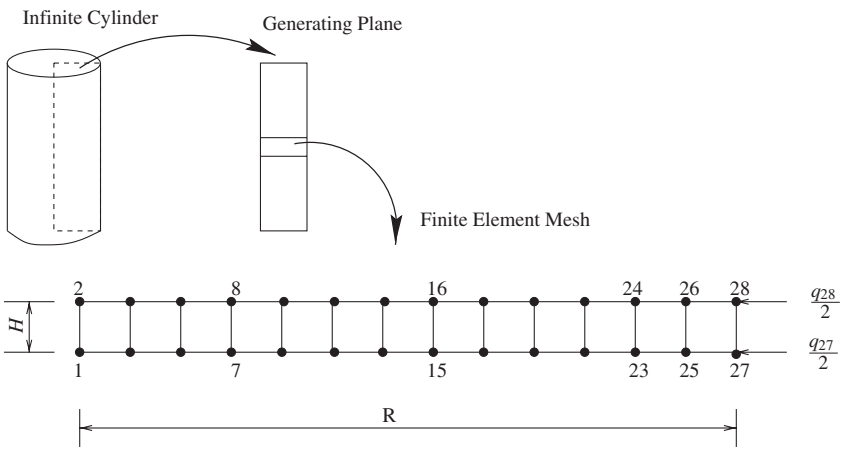

Figure 1. Finite element mesh for the long solid cylinder problem considered in Section 3.

problem described in Section 4 are given in Appendix A. Finally, note that in all cases, heat transfer coefficients at the surface are computed at each time step using

$$h_P^{n+1} = \frac{-q_P^{n+1}}{\theta_P^{n+1} - \theta_\infty} \tag{44}$$

where θ_∞ is the ambient temperature and P is an appropriate global node number.

3.3. Early-time resolution and solution sensitivity as a function of measurement site location

Solutions to inverse heat conduction problems, particularly problems involving highly transient surface heat transfer, must confront two significant physical constraints. First, a diffusional time lag, $\tau_r = \Delta r^2/\alpha$, characterizing the time required for detectable thermal information to diffuse to a subsurface measurement site at depth Δr, must be accommodated. Initial and subsequent surface thermal variations occuring on time scales significantly shorter than τ_r cannot be reconstructed. Second, due to diffusional smearing, transient temperature responses at internal measurement sites diminish significantly compared to thermal variations at the surface. This effect impacts the sensitivity of interior (measured and computed) temperatures to (actual and simulated) surface heat transfer.

In order to examine resolution of early-time surface heat transfer as a function of measurement location, we obtained a series of inverse solutions using single pairs of measurement sites located at varying depths below the cylinder surface. Consistent with experimental conditions described below, the cylinder is assumed to be composed of Inconel 600 and is again given a radius of 6.5 mm. As shown in Figure 2, predicted heat transfer coefficients exhibit large oscillations during the earliest part of the solution. [Note, since temperature decays monotonically in time, the plots in Figures 2, 3, 5, 6, and 8 also indicate the heat transfer coefficient's evolution in time, where highest temperatures occur first. Note too that estimated $h's$ plotted in all figures are instantaneous averages from nodes 27 and 28 in Figure 1; in all cases, these are essentially equal.] However, at some instant, which we denote as τ_{cri},

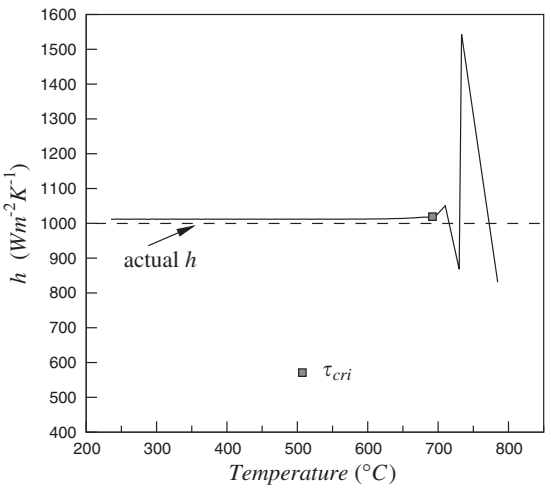

Figure 2. Example of initial oscillation and selection of τ_{cri}.

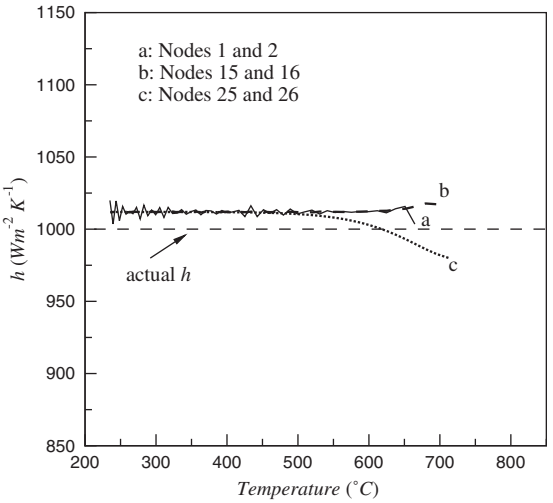

Figure 3. Predicted heat transfer coefficients as functions of temperature for various measurement locations.

and define as the instant when $\Delta\bar{h} = |h_P^{n+1} - h_P^n|/h_P^n \leqslant \varepsilon_h$ $(=0.05)$, the oscillations largely cease and a more or less steady solution sets in. This behaviour is observed at all measurement sites, with the initial oscillatory period persisting longer as measurement site depth increases. This latter feature, which reflects the difficulty of resolving initial surface heat transfer on time scales shorter than τ_r, is depicted in Figure 3, where h estimates prior to τ_{cri} have been removed. In order to quantify this behaviour, we plot τ_{cri} versus τ_r in Figure 4 and use a

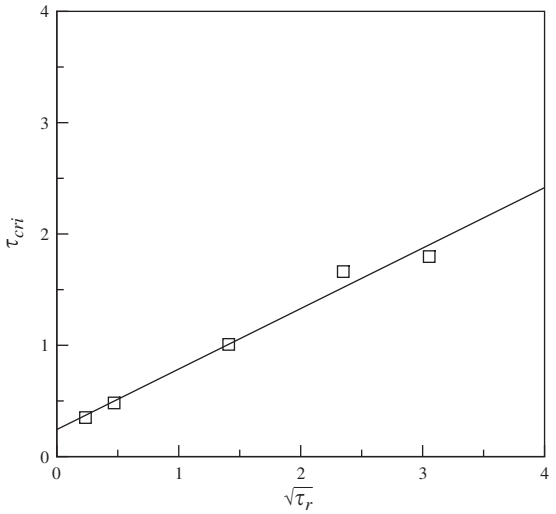

Figure 4. The relationship between τ_{cri} and τ_r.

linear least squares fit to find that

$$\tau_{\text{cri}} = 0.54\sqrt{\tau_r} + 0.24 \tag{45}$$

where the coefficient multiplying $\sqrt{\tau_r}$ has units of $s^{1/2}$. Since τ_r thus varies quadratically with measurement location, Δr, this relationship shows that temporal resolution of initial conditions, characterized by τ_{cri}, decreases linearly with Δr. Although the difficulty of resolving early heat transfer is well recognized, it does not appear that an explicit relationship between achievable resolution and diffusion time has been reported.

With regard to solution sensitivity, we found that in the present problem, inverse solutions are sensitive only to measurements from sites nearest the surface. For example, inverse solutions obtained using sites 25 and 26 alone (Figure 1) are essentially identical to those obtained using all ten sites. Likewise, solutions obtained using, e.g. nodes 15 and 16 alone are largely identical to those obtained using nodes 1, 2, 7, 8, 15, and 16. As expected, and as shown by Equation (45), resolution of initial surface conditions decreases with increasing depth to the nearest subsurface measurement sites.

Finally, note that the approximate 1% discrepancy between estimated and actual h values reflects both spatial and temporal discretization error. In the first instance, truncation error between exact and computed surface heat fluxes is on the order of the outer-most element's radial length (using linear elements) [9]. Inverse solutions obtained using a graduated mesh (having the same number of elements, but with highest resolution near the surface) reduces this difference to less than $\backsim 0.5\%$. The genesis and effect of temporal error requires more explanation. Here, it is observed that estimated surface heat fluxes follow a step-wise decay in time (during cooling), where the length of each step equals the time step size, Δt. Defining incremental surface heat loss as $\Delta Q^{n+1}(\Delta t) = \int_{t^n}^{t^n+\Delta t_{\max}} q(t;\Delta t)\,\mathrm{d}t$, where $\Delta t_{\max}$ is the largest time step tested and time $t^n > \Delta t_{\max}$, it is found that due to increasing temporal resolution,

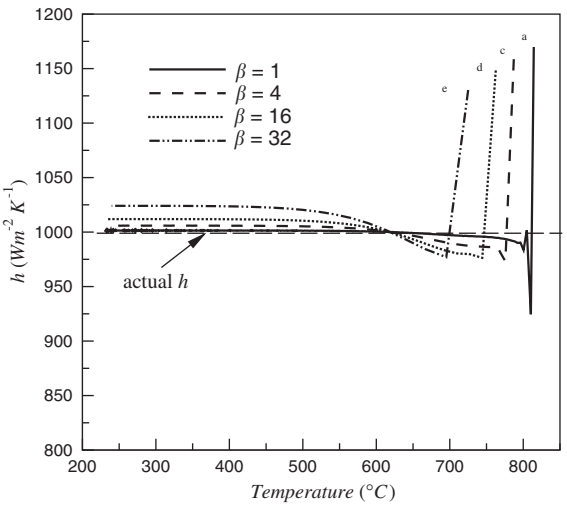

Figure 5. Sensitivity of estimated heat transfer coefficient to solution time step.

$\Delta Q^{n+1}(\Delta t)$ increases with decreasing Δt; indeed, $\Delta Q^{n+1}(\Delta t)$ approaches the actual incremental loss as Δt becomes small (result not shown). As a consequence of conservation of energy, the inverse procedure compensates for this effect by slightly over-predicting the flux magnitude at $t = t^n + \Delta t_{\max}$; the degree of over-prediction increases with increasing Δt. Thus, due to both this feature and the fact that corresponding surface temperature estimates decrease (due to increasing heat loss), h estimates increase with increasing Δt. In the present circumstance, since the cooling curves (of surface heat flux versus time) approach the exact cooling curve as $\Delta t \to 0$, it is clear that estimated values of h will always be greater the actual h and that the mismatch will increase with increasing Δt. See Section 3.4 for further elaboration of this point.

3.4. Sensitivity to solution time step

Similar to the physical constraints limiting resolution of early heat transfer, subsequent time resolution, Δt_R, in an inverse solution is again essentially determined by the diffusive time scale, τ_r. Beck *et al.* [2] have shown how future temperatures can improve somewhat on this fundamental limit, obtaining $\Delta t_R = c\tau_r$, where $c < 1$; however, use of time steps substantially smaller than τ_r invariably leads to solution instability. In order to examine solution accuracy and stability as a function of time step, Δt was varied from Δt_E to $16\Delta t_E$, where Δt_E $(= 0.40\tau_D)$ is again the reciprocal data sample rate. All solutions are based on simulated measurements from the two outer-most measurement sites in Figure 1; thus, $\tau_r = \tau_D = 5.52 \times 10^{-2}$ s.

As shown in Figure 5, stable solutions are obtained over the entire range of time steps tested. Although each solution is initially oscillatory, in every case the oscillations cease after the first six time steps. Subsequent h estimates settle to nominally constant values. Clearly, resolution of early-time heat transfer improves with decreasing time step size. As discussed above, the observed increase in estimated h with increasing Δt arises due to the combined

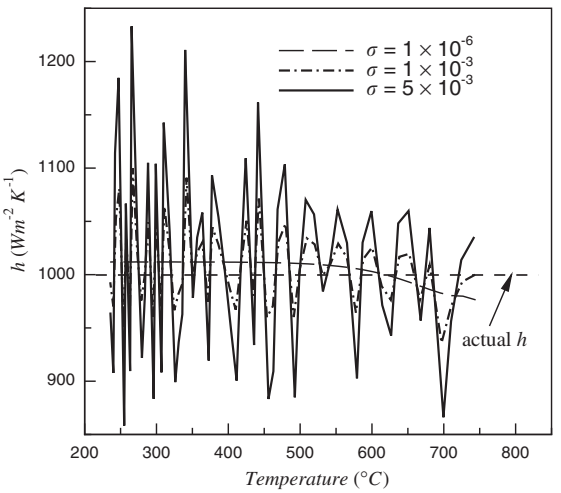

Figure 6. The sensitivity of the estimated heat transfer coefficient to measurement noise.

effects of energy conservation and reduced temporal resolution. Again, this feature, which leads to slight overestimates of incremental heat loss and concommitant underestimates of surface temperature, produces h estimates that increase with increasing Δt.

3.5. Sensitivity to measurement errors

In order to assess the effect of measurement uncertainty on inverse solution accuracy, noisy measurements were simulated by adding a random component to computed temperatures

$$\tilde{Y}_i^{n+1} = \tilde{Y}_{C_i}^{n+1}(1 + \varepsilon_i^{n+1}) \tag{46}$$

where, $\tilde{Y}_i^{n+1}$ is the $(n+1)$th noisy temperature at measurement location i, ε_i^{n+1} is the corresponding random error component, and $\tilde{Y}_{C_i}^{n+1}$ is again determined by (37). The error ε_i^{n+1} is generated using a Gaussian probability distribution, given by Reference [10]

$$\varepsilon_i^{n+1} = \sigma\left(\sum_{l=1}^{12} R_l - 6.0\right) \tag{47}$$

where R_l is a random number uniformly distributed between 0 and 1. Solution accuracy is determined at three levels of error, $\sigma = 10^{-6}$, 10^{-3} and 5×10^{-3}, where the first σ value simulates 'exact' temperature data [2], and where the last two values provide measurement uncertainties on the order of 0.6% and 3%, respectively. As shown in Figure 6, relatively accurate solutions can be obtained at all levels of error. Indeed, predicted histories corresponding to 'exact' temperatures ($\sigma = 10^{-6}$) are essentially indistinguishable from solutions obtained using noise-free measurements ($\sigma = 0$; results not shown). Although solutions become increasingly oscillatory as noise increases, they remain Lyapunov stable (i.e. bounded [2]), even when measurement uncertainty is relatively large. Although not tested, it is expected that regularization would reduce oscillation amplitudes.

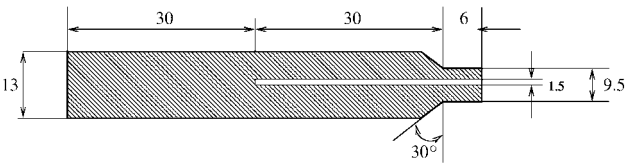

Figure 7. A schematic of the probe used in experiments. All dimensions in mm.

In closing this section, we mention that in linear problems (in which **M** and **K**, and thus $\tilde{\mathbf{X}}$ are constant), error in surface flux estimates can be readily obtained using propagation of error. Thus, from Equations (57) and (59) in Appendix A, we obtain

$$\sum_{i=1}^{I}(\tilde{X}_{i,1})^2\delta\tilde{q}_1^{n+1}+\sum_{i=1}^{I}(\tilde{X}_{i,1}\tilde{X}_{i,2})\delta\tilde{q}_2^{n+1}=\sum_{i=1}^{I}\delta\tilde{Y}_i^{n+1}\tilde{X}_{i,1}-\sum_{i=1}^{I}\delta\tilde{\psi}_i^n\tilde{X}_{i,1} \tag{48}$$

$$\sum_{i=1}^{I}(\tilde{X}_{i,1}\tilde{X}_{i,2})\delta\tilde{q}_1^{n+1}+\sum_{i=1}^{I}(\tilde{X}_{i,2})^2\delta\tilde{q}_2^{n+1}=\sum_{i=1}^{I}\delta\tilde{Y}_i^{n+1}\tilde{X}_{i,2}-\sum_{i=1}^{I}\delta\tilde{\psi}_i^n\tilde{X}_{i,2} \tag{49}$$

where the uncertainty $\delta\tilde{\psi}_i^n$ depends on, and is determined by, the set of previously determined flux uncertainties, $\delta\tilde{q}_1^1,\delta\tilde{q}_2^1,\ldots,\delta\tilde{q}_1^n,\delta\tilde{q}_2^n$.

4. APPLICATION TO QUENCHING PROBLEMS

4.1. Experiments

Determining surface heat transfer during quenching represents a substantial inverse heat transfer problem. Initially, at high part temperatures, a vapour blanket can rapidly form around the part. Depending on the part's size and thermal properties and the quenchant's boiling point, latent heat of vapourization, and ambient pressure, the blanket can persist or quickly collapse. Once the blanket collapses, heterogeneous, turbulent two-phase (nucleate boiling) heat transfer sets in, and eventually gives way to single-phase natural convection.

Quenching experiments were performed using a Drayton Quenchalyzer [11]. Here, an Inconel 600 metal cylinder, having a thermocouple at its geometric centre, as depicted in Figure 7, is heated in a furnace to a prespecified temperature, $\theta_0=850°\text{C}$. Once a steady temperature is achieved, the cylinder is quickly transfered to a stagnant oil bath at $\theta_\infty=40°\text{C}$. Throughout, transient temperature changes at the centre of the probe are acquired and stored by a computerized data acquisition system, sampling at a rate of 8 Hz for a period of 60 seconds.

4.2. Results using non-iterative inverse finite element method

Since the ratio of the probe's half length to its radius is around 5, it suffices to model the probe as a long solid cylinder and to neglect the influence of end heat fluxes. Thus, as mentioned, the FEM direct model described above can be used here, subject to one modification.

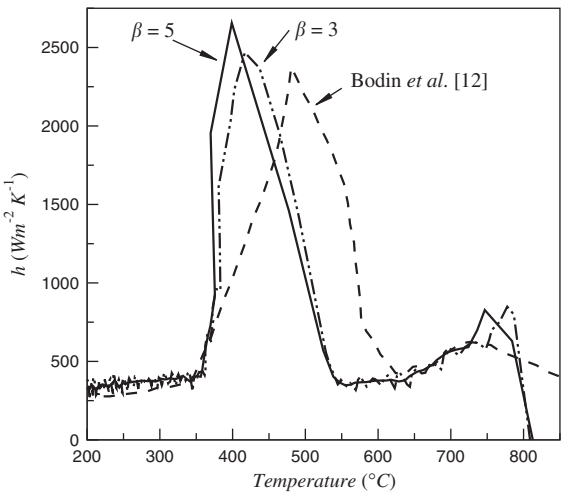

Figure 8. Estimated heat transfer coefficients during quenching for two different sampling rates. Also shown is a comparison with the results of Bodin *et al.* [12].

The modification is needed since only one temperature measurement is available at each time step ($I=1$); since stable inverse solutions cannot be obtained when the number of unknown parameters (K) exceeds the number of measurement sites, the instantaneous flux distribution at global nodes 27 and 28 in Figure 1 is parameterized using only one flux parameter, $\tilde{q}_1^{n+1}$. This change does not violate the essential physics of the problem since relatively uniform heat transfer is expected along the cylinder's periphery. Since non-linearity is important in this problem, quasilinearization is used to account for temperature dependent thermal conductivity and specific heat.

Figure 8 shows typical results when the solution time steps are $3\Delta t_E$ and $5\Delta t_E$, respectively, where Δt_E ($=0.125$s) is again the reciprocal data sample rate. Also shown is a solution reported by Bodin *et al.* [12] using a finite difference-based inverse method and an essentially identical experimental set-up. Consistent with earlier work [4], estimated heat transfer coefficients become oscillatory when the step size equals Δt_E and are not shown. Likewise, initial oscillations, again reflecting under-resolution of early surface heat transfer, and limited to the first 2 or 3 time steps, are removed from the figure.

It is clear that solutions obtained by the present method are qualitatively and quantitatively consistent with those obtained by Bodin *et al.* [12]. Considering first the qualitative features exhibited in Figure 8, the cylinder is initially enveloped in a vapour blanket over $850°\text{C} \gtrsim \theta \gtrsim 560°\text{C}$, with corresponding heat transfer coefficients remaining relatively small. The blanket then collapses, giving way to heterogeneous surface boiling and a rapid increase in surface heat transfer (beginning at $\theta \approx 560°\text{C}$). Gradual suppression of two-phase heat transfer, reflected in the subsequent decay in h, occurs over $400°\text{C} \gtrsim \theta \gtrsim 350°\text{C}$. Finally, natural convection sets in over $350°\text{C} \gtrsim \theta \gtrsim 200°\text{C}$. Quantitatively, the present solution indicates that h reaches a maximum near 440°C while Bodin's solution indicates a maximum at $\theta = 490°\text{C}$. Inspection of the experimental temperature record in Figure 9, however, suggests that since temperature drops from 490°C to 440°C in less than 2 s, both estimates indicate

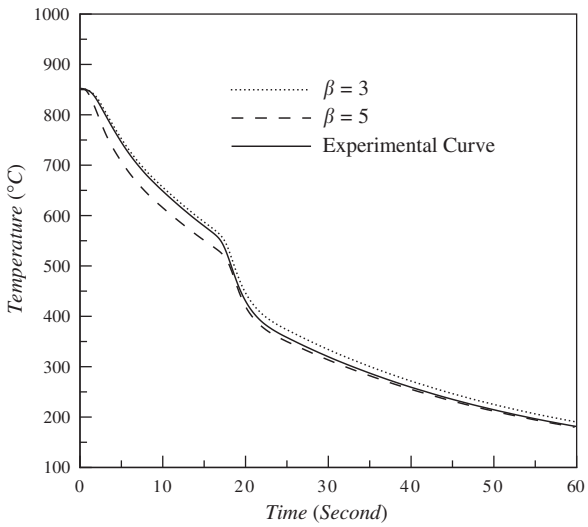

Figure 9. Comparison of computed and experimental temperature histories. The calculated history is obtained using ABAQUS [13]. The time-varying heat transfer coefficient is estimated by the non-iterative inverse finite element method.

h maxima at approximately the same instant. Note too that the large transient increase in h occurs over approximately the same temperature interval in both cases ($560°\mathrm{C} \gtrsim \theta \gtrsim 350°\mathrm{C}$) and that maximum magnitudes are approximately equal. Finally, note that consistent with the discussion in Section 3.4, estimates of maximum h increase with increasing solution step-size.

As an alternative means of accessing inverse solution accuracy, we reformulated the FEM direct model described in Section 3.2 using ABAQUS/Standard 5.8 [13]. Here, estimated h's obtained by the inverse finite element method were used to first define time-dependent flux boundary conditions; corresponding temperatures at the centre of the probe were then calculated. As shown in Figure 9, predicted temperature histories follow the actual data fairly well, with relative errors remaining less than 3% through most of the experiment and increasing to approximately 5% only near the end of the experiment. The effect of solution time-step size, Δt, is also shown in Figure 9. As expected, due to decreasing temporal resolution, relative errors increase to approximately 9% when $\Delta t = 5\Delta t_E$.

5. CONCLUSIONS

A non-iterative finite element method for estimating surface heat flux histories has been developed. Based on the linearity of the unknown flux vector, $\mathbf{q}^{n+1}$, within the direct FE model, minimization of the instantaneous least square error norm leads to a linear system in the parameterized flux, $\tilde{\mathbf{q}}^{n+1}$. The matrix normal equation thus obtained extends application of non-iterative inverse solution techniques to linear and non-linear, multidimensional FEM-based problems. Combined with a closed form expression for the sensitivity coefficient matrix, the

method may eventually prove useful in control and reconstruction applications requiring fast inverse solutions.

The method is validated using independent simulated data from an analytical quenching model; tests using exact data show that estimated heat transfer coefficients remain within 1% of the actual value over most of the simulated experiment. Noisy measurements lead to oscillatory, though stable (bounded) inverse solutions. A modified algorithm, designed to improve system conditioning using data from a future time step, is developed and tested; use of regularization to circumvent ill-conditioning is also briefly discussed. Since the technique must be capable of resolving highly transient surface heat transfer during quenching, particular attention is given to determining early time resolution; it is found that resolution is proportional to the square root of the diffusive time scale between the surface and the nearest subsurface measurement site.

Once validated, the method is used to investigate transient heat transfer during experimental quenching of a cylindrical rod. Comparison with an earlier finite difference-based inverse analysis of a similar experiment shows that the present technique provides flux histories that are in qualitative and quantitative agreement with the earlier approach. Although the present technique is illustrated using a simple one-dimensional example, the method can be extended to multidimensional problems.

APPENDIX A

In order to illustrate some of the details underlying the inverse formulation, we provide intermediate results associated with the test problem described in Section 3.2. Again, the objective is to solve for q_{27}^{n+1} and q_{28}^{n+1}, which are not necessarily equal. Since $\mathbf{c}=\mathbf{0}$, only the outer-most element (shown in Figure A1) contributes to the formation of the force vector.

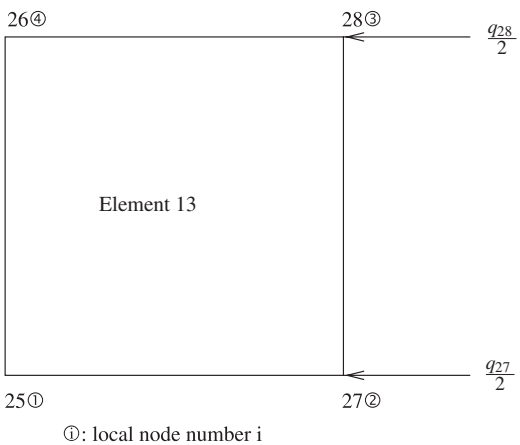

Figure A1. Local numbering for element 13 in the mesh for the test problem considered in Section 3.2.

Specifically, the only non-zero vector elements are f_{27}^{n+1} and f_{28}^{n+1}, given by

$$f_{27}^{n+1} = \int_{\Gamma_2} qN_2 \, \mathrm{d}S = RH \left(\frac{2\tilde{q}_1^{n+1} + \tilde{q}_2^{n+1}}{6} \right) \tag{A1}$$

$$f_{28}^{n+1} = \int_{\Gamma_2} qN_3 \, \mathrm{d}S = RH \left(\frac{\tilde{q}_1^{n+1} + 2\tilde{q}_2^{n+1}}{6} \right) \tag{A2}$$

where 2π has been canceled out of all terms and where $\tilde{q}_1^{n+1} = q_{27}^{n+1}$ and $\tilde{q}_2^{n+1} = q_{28}^{n+1}$. Thus,

$$\mathbf{f}^{n+1} = \frac{RH}{6} \left[0, \ldots, 0, 2\tilde{q}_1^{n+1} + \tilde{q}_2^{n+1}, \tilde{q}_1^{n+1} + 2\tilde{q}_2^{n+1} \right]^{\mathrm{T}} \tag{A3}$$

Given $\mathbf{f}^{n+1}$ $\tilde{\mathbf{D}}$ can be determined using (23):

$$\tilde{\mathbf{D}} = \frac{RH}{6} \begin{bmatrix} 0 & 0 \\ 0 & 0 \\ . & . \\ . & . \\ . & . \\ 2 & 1 \\ 1 & 2 \end{bmatrix} \tag{A4}$$

where the dimensions of $\tilde{\mathbf{D}}$ are 28×2. Similarly, given $\tilde{\mathbf{D}}$, $\tilde{\mathbf{X}}$ follows from (25)

$$\tilde{X}_{i,1} = \frac{RH\Delta t_0}{6} (2\tilde{U}_{i,27} + \tilde{U}_{i,28}) \tag{A5}$$

$$\tilde{X}_{i,2} = \frac{RH\Delta t_0}{6} (\tilde{U}_{i,27} + 2\tilde{U}_{i,28}) \tag{A6}$$

Thus, using the last two expressions in (24) gives

$$\tilde{\theta}_i^{n+1} = \tilde{\psi}_i^n + (\tilde{X}_{i,1}\tilde{q}_1^{n+1} + \tilde{X}_{i,2}\tilde{q}_2^{n+1}) \quad i = 1, 2, \ldots, I; \quad I = 2, 4, \ldots, 10 \tag{A7}$$

so that minimization of S^{n+1} with respect of $\tilde{q}_1^{n+1}$ yields

$$\sum_{i=1}^{I} (\tilde{X}_{i,1})^2 \tilde{q}_1^{n+1} + \sum_{i=1}^{I} (\tilde{X}_{i,1}\tilde{X}_{i,2}) \tilde{q}_2^{n+1} = \sum_{i=1}^{I} (\tilde{Y}_i^{n+1} - \tilde{\psi}_i^n) \tilde{X}_{i,1} \tag{A8}$$

Similarly, calculating

$$\frac{\partial S^{n+1}}{\partial \tilde{q}_2^{n+1}} = 0 \tag{A9}$$

gives

$$\sum_{i=1}^{I}(\tilde{X}_{i,1}\tilde{X}_{i,2})\tilde{q}_1^{n+1}+\sum_{i=1}^{I}(\tilde{X}_{i,2})^2\tilde{q}_2^{n+1}=\sum_{i=1}^{I}(\tilde{Y}_i^{n+1}-\tilde{\psi}_i^n)\tilde{X}_{i,2} \tag{A10}$$

Together, (A8) and (A10) comprise two equations in the two unknown fluxes, $\tilde{q}_1^{n+1}$ $(=q_{27}^{n+1})$ and $\tilde{q}_2^{n+1}$ $(=q_{28}^{n+1})$.

ACKNOWLEDGEMENTS

Discussions with Mr Jianpeng Feng are greatly appreciated. This work was supported by the National Science Foundation, Grant No. DMI-9820880.

REFERENCES

1. Özisik MN, Orlande HRB. *Inverse Heat Transfer*. Taylor and Francis: New York, 2000.
2. Beck JV, Blackwell B, St. Clair CR. *Inverse Heat Conduction: Ill-Posed Problems*. Wiley Interscience: New York, 1985.
3. Tikhanov AN, Arsenin VY. *Solution of Ill-Posed Problems*. Winston & Sons: Washington, DC, 1977.
4. Keanini RG. Inverse estimation of surface heat flux distribution during high speed rolling using remote thermal measurement. *International Journal of Heat and Mass Transfer* 1998; **41**:275–285.
5. Trujillo DM, Busby HR. *Practical Inverse Analysis in Engineering*. CRC Press: Boca Raton, 1997.
6. Johnson RE, Keanini RG. An asymptotic model of work roll heat transfer during strip rolling. *International Journal of Heat and Mass Transfer* 1998; **41**:871–879.
7. Keanini RG. Review: reconstruction and control of phase boundaries during fusion welding. *Trends in Heat, Mass and Momentum Transfer* 1997; **3**:139–145.
8. Carslaw HS, Jaeger JC. *Conduction of Heat in Solids*. Clarendon Press: Oxford, 1959.
9. Reddy JN. *An Introduction to the Finite Element Method*. McGraw-Hill: New York, 1984.
10. Xu SL. *Collection of Common Algorithms in Fortran*. Tsinghua University Press: Beijing, 1995.
11. *Quenchalyzer Manual*, Instruments & Technology, Inc., 2000.
12. Bodin J. Segerberg S. Benchmark testing of computer programs for determination of hardening performance. In *Quenching and Distortion Control*, George E. Totten (ed). ASM International, 1992.
13. *ABAQUS Users' Manual*, v-5.8, Hibbitt, Karlsson and Sorensen, 1998.

